# Spatial Resolution Properties in Penalized-Likelihood Reconstruction of Blurred Tomographic Data

Wenying Wang, Grace J. Gang and J. Webster Stayman
Department of Biomedical Engineering, Johns Hopkins University, Baltimore, MD

***Abstract*— The understanding of the image properties produced by a medical imaging system is critical to effective interpretation of the diagnostic images they produce. Quantitative analysis of image properties like spatial resolution can be complex in computed tomography when advanced model-based reconstruction methods like penalized-likelihood estimation are used since spatial resolution is dependent on patient anatomy, x-ray exposures, and location in the field of view. Previous work [1] has derived mathematical expressions for the local impulse response which quantifies spatial resolution and permits prospective analysis, control, and optimization of the imaging chain including tuning of the reconstruction algorithm. While previous analysis is appropriate for many diagnostic systems, it relies on an idealized system model that ignores any projection blur. Newer devices including cone-beam CT systems that utilize flat-panel detectors can experience significant system blur both due to light spread in the scintillator and due to extended x-ray focal spots. This work introduces a derivation of the local impulse response for penalized-likelihood reconstruction where projections are subject to system blur. We investigate the new local impulse response expression in both simulation studies and in physical test-bench experiments, demonstrating the accuracy of this new resolution predictor.**

***IndexTerms*–Local impulse response, penalized likelihood reconstruction, flat panel cone-beam CT**

## I. INTRODUCTION

The past decade has seen rapid development in computed tomography (CT) both in hardware implementation and reconstruction algorithm design. Cone-beam CT (CBCT) systems based on flat-panel detectors have found widespread use in a number of medical applications including dedicated point-of-care scanners, mobile devices, and interventional imaging systems. Model-based iterative reconstruction (MBIR) algorithms are also finding increased clinical use and are an important tool for dose reduction in diagnostic CT. Such algorithms are also finding application in flat-panel-based CBCT.

MBIR approaches often take advantage of a statistical model of the measurement data to weigh the relative contribution of different measurements. These statistical weights are data-dependent and can lead to varying image properties in reconstructions of different patients and different anatomical sites. For example, in penalized-likelihood (PL) reconstructions of tomographic data, the interaction between the data fidelity term (which contains the statistical model) and a standard shift-invariant penalty term leads to resolution properties that are shift-variant. In this scenario, more blur is typically induced in regions where data fidelity is lower (e.g. near more dense tissues in CT) and less blur where data fidelity is higher (e.g., at patient skin-air boundaries).

Corresponding author: J. Webster Stayman (email:web.stayman@jhu.edu)

This behavior was examined analytically by Fessler in [1] where expressions for local noise and resolution properties were derived based on Taylor approximation. Those expressions characterize the dependence of image properties on the position in the field of view, the patient anatomy including the local attenuation values, the x-ray technique (i.e., exposure), the system geometry, and the regularization/penalty used in the penalized-likelihood objective function. Recent work has explored highly computationally efficient methods for computing the local noise and resolution properties.[2]

Such analytic tools permit the prospective prediction of image properties without having to explicitly reconstruct tomographic data. With this ability, one can optimize data acquisitions and reconstruction strategies (e.g. regularization) for specific goals and consistent behavior across scanning conditions. Previously, such predictors have been used to enforce uniform spatial resolution properties in reconstructions [3] or to maximize imaging performance through computations of the local detectability index (which is a function of local noise and resolution) for specific imaging tasks through customization of the source-detector trajectory [4], modulation of the tube current as a function of rotation angle [5], and space-variant design of regularization. [6], [7]

To our knowledge, all previous work on the prospective prediction of imaging properties for MBIR has presumed an idealized system without system blur. More specifically, it is assumed that the x-ray source is small relative to detector pixels so that focal spot blur is negligible; and that there is little to no sharing of signal between detector pixels. While this assumption has historically worked well enough for current clinical scanners, this may be a poor assumption for high-spatial-resolution CT applications and CBCT systems based on flat-panel detectors. In particular, focal spot effects may be more important for higher resolution systems and the assumption of no signal sharing between pixels is inappropriate for many flat-panel detectors. For example, in indirect detection flat panels, there is a scintillator layer that converts single X-ray photons into many visible photons, which typically spread spatially over multiple pixels. This light spreading is often relatively large compared to the pixel size, meaning that detector blur can have a significant impact on the overall resolution properties of a CBCT system. [8]

In this work, we focus on the derivation of a predictor for the spatial resolution properties of PL-reconstructed CBCT

data with non-ideal detectors exhibiting spatial blur. While recent work has attempted to model such blur in the forward model as part of the reconstruction [9], this work is concentrated on predicting resolution properties for a standard reconstruction forward model (without blur) that is applied to data that contains systemic blur. We follow the general general methodology presented by Fessler[1] to derive the prospective predictor, and then verify its accuracy in both simulation and physical test-bench studies.

## II. METHODS

### A. Penalized-Likelihood Reconstruction

While there are many different MBIR approaches that have been proposed, PL methods have a number of advantages including the weighting of individual measurements by their statistical fidelity, a variety of fast algorithms for iterative estimation, and their relative amenability to mathematical analysis. Unlike direct analytical reconstruction methods, PL reconstruction is typically posed as the solution of an implicitly defined objective function, and generally does not have a closed-form expression. Consider the following implicitly defined estimator:

$$\hat{\mu} = \arg\max_{\mu} \Phi(\mu, y) \tag{1}$$

where $\mu \in \mathbb{R}_+^{N\times 1}$ denotes a vector of attenuation coefficients representing the image volume and $y \in \mathbb{R}_+^{P\times 1}$ is the vector of tomographic measurements made by the CT scanner. The estimate, $\hat{\mu}$, is the image that maximizes the value of the objective $\Phi$. For a PL objective

$$\Phi(\mu, y) = L(\mu, y) - \beta R(\mu) \tag{2}$$

$$L(\mu, y) = \sum_i y_i \log \bar{y}_i(\mu) - \bar{y}_i(\mu) \tag{3}$$

where $L$ is the likelihood function and $R$ is a roughness penalty whose relative strength is controlled by the parameter $\beta$. In this work, we focus on quadratic penalties on pairwise voxel differences. Equation (3) is the likelihood function presuming Poisson measurement data which is a function of the mean measurement model $\bar{y}$. The typical forward model for $\bar{y}$, which we will adopt here for reconstruction, is

$$\bar{Y}_{\text{recon}}(\mu) = I_0 \exp(-\mathbf{A}\mu) \tag{4}$$

where $\mathbf{A} \in \mathbb{R}_+^{P\times N}$ is ideal forward-projector system matrix and $I_0$ denotes a scalar gain term specifying the bare-beam fluence level. It is important to differentiate between the idealized reconstruction model and the true physical model through which data is obtained. For example, a more accurate physical model will include system blur. For example, introducing a blur model for projection data acquisition, one may write

$$\bar{Y}_{\text{acq}}(\mu) = \mathbf{B} I_0 \exp(-\mathbf{A}\mu) \tag{5}$$

where $\mathbf{B} \in \mathbb{R}^{P\times P}$ denotes a blur operator. We seek to predict resolution properties of images reconstructed using PL with the traditional forward model of (4) but with data that was obtained with blur in the detection process as in (5).

### B. Spatial Resolution in Penalized-Likelihood Images

It is well known that PL reconstruction of CT data with standard space-invariant penalties yields nonuniform resolution properties that are dependent on the x-ray technique, geometry, and patient anatomy. However, with quadratic penalties resolution properties are locally linear and shift-invariant - making a local impulse response a valuable analytic tool. Local impulse response, by definition, is the relative change of reconstructed result from a small local increase in ground truth. The local impulse response of the $j$th voxel can be written as,

$$l_j = \lim_{\delta\to 0} \frac{\hat{\mu}(\bar{y}(\mu + \delta e_j)) - \hat{\mu}(\bar{y}(\mu))}{\delta} = \frac{\partial}{\partial \mu_j} \hat{\mu}(\bar{y}(\mu)) \tag{6}$$

$$= \nabla_y \hat{\mu}(\bar{y}(\mu)) \frac{\partial}{\partial \mu_j} \bar{y}(\mu) \tag{7}$$

where $e_j$ denotes a vector with all zeros except for the $j^{th}$ element that is unity.

In PL reconstruction, $\hat{\mu}$ is estimated with the forward projection model (without blur) in (4) but with $\bar{Y}_{\text{acq}}$ as its argument. Thus, the first term in (7) is written as

$$\nabla_{\bar{Y}_{\text{acq}}} \hat{\mu}(\bar{Y}_{\text{acq}}) = [-\nabla^{20}\Phi(\mu, \bar{Y}_{\text{acq}})]^{-1} \nabla^{11}\Phi(\mu, \bar{Y}_{\text{acq}}) \tag{8}$$

$$= [\mathbf{A}^T D[I_0 \text{exp}(-\mathbf{A}\hat{\mu}(\bar{Y}_{\text{acq}}))]\mathbf{A} + \mathbf{R}]^{-1}\mathbf{A}^T \tag{9}$$

where $\mathbf{R} = \nabla^2 R(\mu)$ the Hessian of the penalty and $\mathbf{D}\{\cdot\}$ denotes an operator that puts its vector argument on the diagonal of a matrix. The second term in (7) may be written

$$\frac{\partial}{\partial \mu_j} \bar{y}(\mu) = \frac{\partial}{\partial \mu_j} \bar{Y}_{\text{acq}}(\mu) \tag{10}$$

$$= -\mathbf{B}\mathbf{D}\{I_0 \exp(-\mathbf{A}\mu)\}\mathbf{A}e_j \tag{11}$$

Combining (9) and (11) into (7) yields

$$l_j = [\mathbf{A}^T\mathbf{W}\mathbf{A} + \mathbf{R}]^{-1}\mathbf{A}^T\mathbf{B}\mathbf{W}_0\mathbf{A}e_j \tag{12}$$

where the two diagonal weighting operators are defined as

$$\mathbf{W} = D[I_0 \text{exp}(-\mathbf{A}\hat{\mu}(\bar{Y}_{\text{acq}}))] \tag{13}$$

$$\mathbf{W}_0 = D[I_0 \text{exp}(-\mathbf{A}\mu)] \tag{14}$$

This expression differs from previous formulations of the local impulse response with the addition of the blur operator, $\mathbf{B}$, before the weighting, $\mathbf{W}_0$ on the right side of the equation due to its presence in the physical forward model in (11). In contrast, $\mathbf{B}$ does not appear in the inverse operation of (9) since the reconstruction model does not include knowledge of system blur. The diagonal weighting operators above are slightly different in form since (13) are weights based on the reprojection of the reconstruction of blurred measurements, whereas (14) does not have this added blur. In practice these additional blurs have a minor effect on the overall estimate since the operator is sandwiched between projection and back-projection operation. In our investigations we approximate both weighting terms using a "plug-in" approach by substituting the actual measurements.

Although an explicit closed-form expression of local impulse response is achieved, the matrix inverse in (12) is computationally cumbersome. Thus, to solve for the response, one can either apply iterative algorithms like conjugate-gradient to estimate (12), or use Fourier methods to give an approximate solution.[3] Specifically, we may compute

$$l_j = \mathscr{F}^{-1}\{\frac{\mathscr{F}\{\mathbf{A}^T\mathbf{B}\mathbf{W}\mathbf{A}e_j\}}{\mathscr{F}\{\mathbf{A}^T\mathbf{W}\mathbf{A}e_j + \mathbf{R}e_j\}}\} \tag{15}$$

where $\mathscr{F}$ and $\mathscr{F}^{-1}$ denote discrete 3D Fourier transforms and inverse transforms, respectively. In this work, we will investigate the accuracy of the expression in (15).

### C. System Blur Measurement

To validate the expression for local impulse response in a system with a realistic blur model, we measured blur in a physical flat-panel based cone-beam CT (CBCT) system. There are two major sources of blur in most CBCT systems with indirect detectors: 1) blur due to light spread in the scintillator, and 2) focal spot blur due to an extended x-ray focal spot. We choose to decompose the total system blur $\mathbf{B}$ into two separable terms, detector blur $\mathbf{B}_d$ and focal spot blur $\mathbf{B}_s$. [11]

$$\mathbf{B} = \mathbf{B}_d\mathbf{B}_s \tag{16}$$

Strictly speaking, this model breaks down for larger objects since source blur is depth-dependent. However, when considering the local impulse response about a location $j$ near the center of rotation, this model is appropriate. (One can imagine extending this idea to use a view-dependent blur that accommodates a varying depth-dependent blur for a particular location if it is not near the center of rotation.)

Following [10], we use a tungsten plate (50 mm $\times$ 50 mm $\times$ 5 mm) to measure systemic blurs in the projection data via an edge response. A presampled edge spread function (ESF) is estimated and differentiated to compute the line spread function (LSF). One-dimensional Fourier transformation of the LSF yields a one dimensional modulation transfer function (1D-MTF) associated with the particular angulation of the tungsten plate. To characterize resolution properties along different orientations, we rotated the tungsten plate over a number of different angles to form additional 1D-MTFs. For estimates of blur due to the detector, the tungsten plate was placed directly on the face of the detector panel (minimizing focal-spot blur). To estimate the total system blur (including both source and detector effects), the tungsten plate/edge was placed at the center of rotation to estimate the projection blur expected for the object.

### D. Validation of the Local Impulse Response Analysis

We evaluate the new local impulse response expression in (15) in two experiments: 1) a simulation experiment where the system blur is exactly known; and 2) physical experiments using a CBCT test-bench. Both experiments use the penalized-likelihood estimator described above in (1) and (3) with a quadratic penalty and first-order neighborhood for pairwise voxel differences. The separable paraboloidal

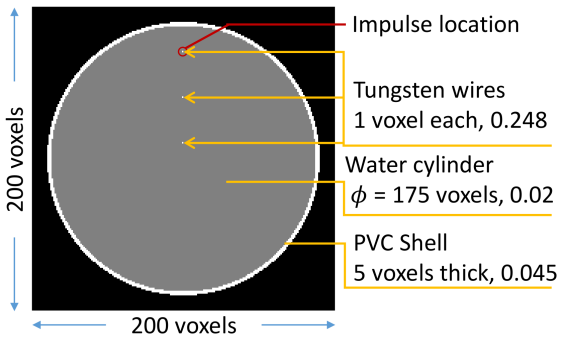


(a) Cross-section of the digital phantom used in simulation studies. The phantom mimics a physical phantom with a PVC shell, water interior, and three tungsten wires. Attenuation coefficients of material are given. Height of the phantom is 50 voxels.

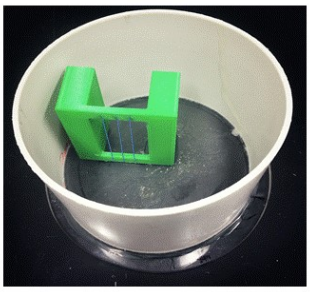

(b) Physical phantom with three tungsten wires attached to green 3D-printed holder. Shown empty but water-filled for data acquisition.

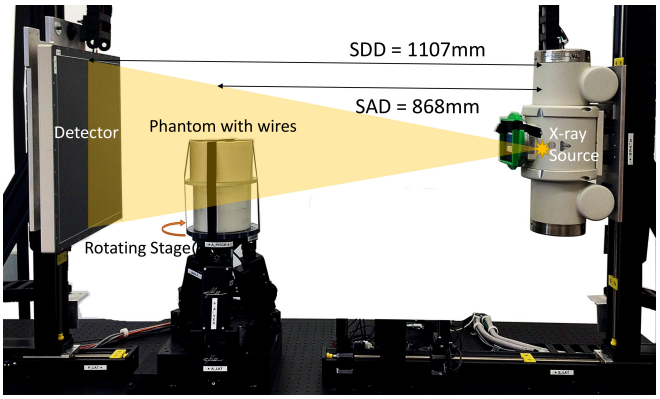


(c) Test bench setup.

Fig. 1: Phantom designs in simulation and bench study.

surrogates (SPS)[12] algorithm is chosen to minimize the PL objective function using 900 iterations and a single subset. All reconstructions used a voxel size of 0.2 mm $\times$ 0.2 mm $\times$ 0.2 mm. Algorithms were coded in MATLAB and include external calls to CUDA-based libraries implementing separable footprints [13] projectors/backprojectors. A 51 voxel $\times$ 51 voxel $\times$ 51 voxel region of interest (ROI) is applied to contain the blur from impulse in both study.

*1) Simulation Study:* For the simulation study, we adopted the digital phantom shown in Figure 1a and generate noiseless projection data using the physical forward model in (5) with following geometry parameters: source-to-axis

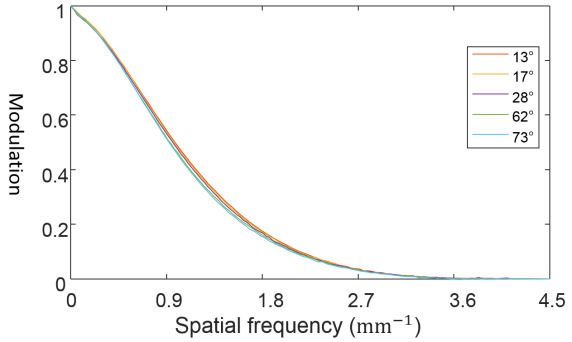


(a) Detectors resolution properties along different orientations. Legend shows angles between edge and vertical grid on detectors panel.

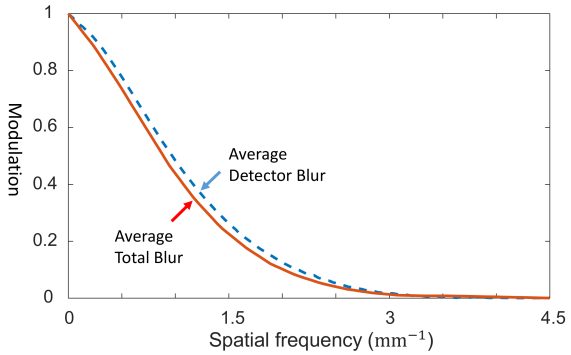


(b) Comparison between total system blur and detector blur.

Fig. 2: MTF Measurements showing blur associated with data collection in the CBCT test-bench.

distance (SAD) = 1107mm, source-to-detector distance (SDD) = 868 mm. X-ray fluence level was set to $I_0 = 18800$ photons in the bare beam. The simulated blur model used the detector blur results from the test-bench experiment. The FWHM width of the measured detector point spread function (PSF) was approximately 0.8 mm and pixel size was 0.278 mm$\times$0.278 mm. We repeated PL reconstructions with and without an impulse in the digital phantom to directly estimate a local impulse response according to (6). This evaluation served as the ground truth response and was compared with the derived local impulse response of (15) over a range of regularization values (sweeping $\beta$ between $10^4$ and $10^6$).

*2) Test Bench Study:* The ability to predict resolution was also evaluated on a physical CBCT test-bench. The test bench consists of a flat panel detector (1536 $\times$ 1536 pixels, pixel size 0.278 mm$\times$0.278 mm), X-ray tube, and a rotating stage which holds objects as shown in Figure 1c. The geometry matched the simulation experiments.

To investigate local spatial resolution properties in physical data, a water-filled cylinder served as a phantom and is shown in Fig. 1b. Three tungsten wires (diameter $\phi$ = 127 $\mu$m) were fixed in a water-filled cylinder container (diameter $\phi$ = 16 cm). These wires are substantially thinner than one voxel making them good approximations to impulses for local resolution estimation. To isolate the system response of a wire, the background water value is calculated within a ring surrounding the wire and subtracted from reconstructed volume. Over 20 slices containing the wire stimuli, we use Gaussian fitting to find the center of the wire. The average (axial) in-plane response over all slices was computed to reduce noise effects. This average represents a 2D line response function which may be compared with a line response formed from the analytic predictor in (15) by integrating the predicted 3D-PSF in the z-direction. An additional circular blur of 127 $\mu$m corresponding to the wire diameter was applied to predictions with and without modeled blur for comparison. Because the attenuation of the wire is not known exactly, measurements are normalized by ensuring the integral of the line spread function is unity.

## III. Results

### A. System Blur Measurement

The results of the physical test-bench blur characterization are shown in Figure 2a. The computed 1D MTFs for five different angles are plotted. We note that the MTF does not vary significantly with orientation suggesting a highly isotropic detector response. Similar investigations across the face of the panel suggested a high degree of detector blur uniformity. For the following simulation investigations these measured MTFs were averaged to form a truly isotropic MTF.

Test-bench experiments used a 0.4 mm focal-spot. Taking magnification into account, we would expect a projection blur of approximately 0.12 mm for an object at the center of rotation. This additional blur due to the source is evident in the MTF measurements made at the center of rotation. In Figure 2b, the MTF for total blur falls off slightly faster than the MTF representing detector blur alone. While source blur effects are relatively small in this test-bench configuration, the (angularly averaged) total blur is used in the following physical data investigations for resolution prediction.

### B. Simulation Study

Fig. 3 shows resolution estimation results for a peripheral location in the simulation phantom. Three different PL regularization parameter strengths were applied from $10^4$ to $10^6$. 2D slices of the 3D PSF and 3D MTF are shown, as well as 1D horizontal profiles through each of these function. Each sub-figure containing a 2D function shows the predicted estimation result on the left side and measurement outcome on the right side for comparison. These PSF and MTF images show very good symmetry indicating that the prediction is consistent with measurement. From the profiles, we can see excellent agreement between measurement and the new predictors that include detector blur. Traditional predictors (without a detector blur model) deviate substantially from the measured results. When regularization strength increased, the PL reconstruction exhibits increased overall blur which reduces this mismatch since resolution properties are dominated by reconstruction blur.

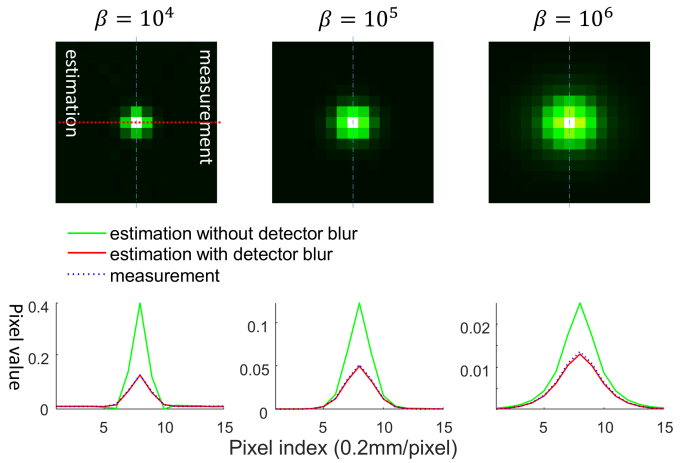


(a) Predicted PSF estimates and direct measurements within a zoomed 15 voxel×15 voxel region of interest.

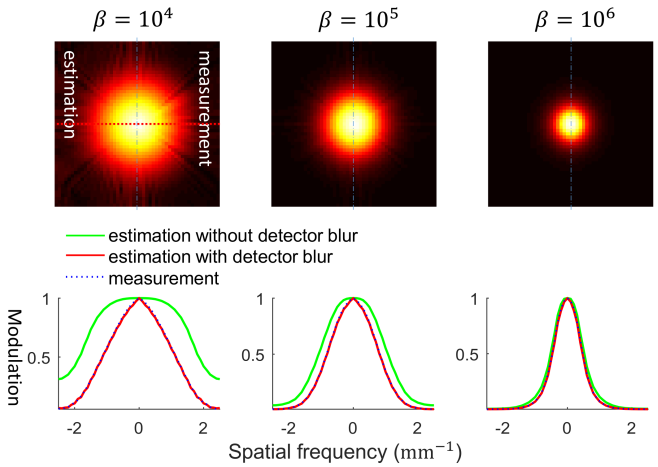


(b) Predicted MTF estimates and direct measurements.

Fig. 3: Simulation study results. Each sub-figure in the upper row shows the prediction on the left and measurement on the right. The lower row shows central horizontal profiles of the 2D results above. Predicted results using previous derivations without a blur model are shown (in green) in the profile plots. The same impulse location is shown for three different regularization parameter ($\beta$) values.

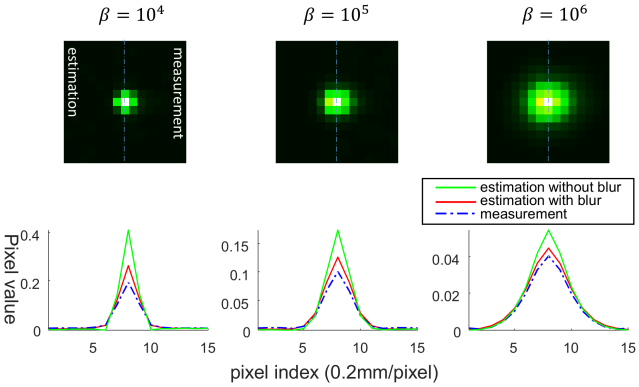


Fig. 4: Test bench study results. PL reconstruction penalty strength $\beta$ from left to right columns:$10^3$, $10^4$, $10^5$. For line spread function estimates for varying $\beta$, summations over the center 5 voxel×5 voxel, 9 voxel×9 voxel, 17 voxel×17 voxel regions are normalized to 1 respectively. Upper: comparison between line spread function estimation and measurement. Zoomed in to center 15 voxel×15 voxel region.Lower: center row profiles comparison between prediction and measurement.

### C. Test Bench Study

Preliminary resolution prediction results for the test-bench are shown in Fig. 4. 2D line spread functions for wire closest to the PVC wall are shown for three different regularization parameters. The 2D functions are organized in the same way as in simulation study with the left half showing the prediction and the right half showing the measurement. Like the simulation study, the results are highly symmetric suggesting good agreement between the predictions and measurements. The horizontal profiles through the measurements and predictions are also shown. We see that including the system blur yields a line spread function that is closer to the measured value than the traditional predictor that does not include blur. In these results there is still a small mismatch (most notable at the peak of the line spread function). The measured blur is still larger than the predicted blur, suggesting that there is residual un-modeled blur in the physical CBCT test-bench. We conjecture that this residual blur is due to slight errors in the geometric calibration of the system. This slight mismatch is the subject of ongoing investigations.

## IV. DISCUSSION

In this paper we presented a novel derivation of the local impulse response for PL reconstruction that includes physical system blurs including non-ideal detectors and source blur that has been ignored in previous derivations. The resolution predictor is similar to previously investigated forms and can be evaluated quickly using local Fourier methods. The approach takes into account the system geometry, measurement statistics, and the object-dependence (but requires only an estimate of the projection data for computation). Measured versus predicted results are nearly identical in simulation studies. In physical testbench experiments, preliminary studies show that the new resolution predictor yields quantitative measures of spatial resolution that are closer than previous predictors that do not model inherent system blurs. We conjecture that residual mismatches between predictions and measurements are the result of un-modeled blurs resulting from an inexactly known geometry.

This work is an important first step in applying predictors of imaging performance in real flat-panel-based CBCT systems. Such predictors are critical for establishing reliable reconstructions (e.g., consistent resolution properties across acquisition methods, x-ray techniques, and patient sizes)

as well as more complex system optimization using task-based image quality metrics. The latter optimization methods generally require predictors for both the spatial resolution and noise properties of the imaging system. We plan on using a similar development to extend this work to noise prediction (e.g., of the local noise power spectrum) for devices with system blur. Thus, this work represents an important building block for the application of MBIR in real CBCT systems for reliable operation and future optimization.

## ACKNOWLEDGEMENTS

This work was supported in part by the National Institutes of Health grant U01EB018758.

## REFERENCES

[1] J. A. Fessler and W. L. Rogers, Spatial resolution properties of penalized-likelihood image reconstruction: Space-invariant tomographs, IEEE Trans. Image Process., vol. 5, no. 9, pp. 13461358, 1996.

[2] S. Schmitt, M. Goodsitt, and J. Fessler, Fast Variance Prediction for Iteratively Reconstructed CT Images with Locally Quadratic Regularization, IEEE Trans. Med. Imaging, vol. PP, no. 99, pp. 1726, 2016.

[3] J. W. Stayman and J. A. Fessler, Regularization for uniform spatial resolution properties in penalized-likelihood image reconstruction, IEEE Trans. Med. Imaging, vol. 19, no. 6, pp. 601615, 2000.

[4] J. W. Stayman, G. J. Gang, and J. H. Siewerdsen, Task-Based Optimization of Source-Detector Orbits in Interventional Cone-beam CT, Fully Three-Dimensional Image Reconstr. Radiol. Nucl. Med. Int. Meet., pp. 5558, 2015.

[5] G. J. Gang, J. H. Siewerdsen, and J. W. Stayman, Task-Driven Tube Current Modulation and Regularization Design in Computed Tomography with Penalized-Likelihood Reconstruction, Phys. Med. Biol. (submitted)

[6] H. Dang et al., Regularization design for high-quality cone-beam CT of intracranial hemorrhage using statistical reconstruction, SPIE Med. Imaging, vol. 9783, p. 97832Y, 2016.

[7] G. J. Gang, J. W. Stayman, W. Zbijewski, and J. H. Siewerdsen, Task-based detectability in CT image reconstruction by filtered backprojection and penalized likelihood estimation., Med. Phys., vol. 41, no. 8, p. 81902, 2014.

[8] W. Zhao, G. Ristic, and J. a Rowlands, X-ray imaging performance of structured cesium iodide scintillators., Med. Phys., vol. 31, no. 9, pp. 25942605, 2004.

[9] S. Tilley II, J. H. Siewerdsen, and J. W. Stayman, Model-based iterative reconstruction for flat-panel cone-beam CT with focal spot blur, detector blur, and correlated noise, Phys. Med. Biol., vol. 61, no. 1, p. 296, 2016.

[10] E. Samei, M. J. Flynn, D. A. Reimann, E. Samei, M. J. Flynn, and D. A. Reimann, A method for measuring the presampled MTF of digital radiographic systems using an edge test device., Med. Phys.,vol. 102, no. 1998, 2012.

[11] S. Tilley II, J. H. Siewerdsen, W. Zbijewski, and J. W. Stayman, Nonlinear Statistical Reconstruction for Flat-Panel Cone-Beam CT with Blur and Correlated Noise Models., Proc. SPIE–the Int. Soc. Opt. Eng., vol. 9783, pp. 19, 2016.

[12] H. Erdogan and J. A. Fessler, Ordered subsets algorithms for transmission tomography, Phys. Med. Biol., vol. 44, no. 11, 1999.

[13] Y. Long, J. A. Fessler, and J. M. Balter, A 3D Forward and Back-Projection Method for X-Ray CT Using Separable Footprint, Med. Imaging, IEEE Trans., vol. 29, no. 11, pp. 36, 2010.